

Microstructures, Martensitic Transformation, and Mechanical Behavior of Rapidly Solidified Ti-Ni-Hf and Ti-Ni-Si Shape Memory Alloys

X.L. Han, K.K. Song , L.M. Zhang, H. Xing, B. Sarac, F. Spieckermann, T. Maity, M. Mühlbacher, L. Wang, I. Kaban, and J. Eckert

(Submitted November 27, 2017; published online February 1, 2018)

In this work, the microstructure and mechanical properties of rapidly solidified $\text{Ti}_{50-x/2}\text{Ni}_{50-x/2}\text{Hf}_x$ ($x = 0, 2, 4, 6, 8, 10,$ and 12 at.%) and $\text{Ti}_{50-y/2}\text{Ni}_{50-y/2}\text{Si}_y$ ($y = 1, 2, 3, 5, 7,$ and 10 at.%) shape memory alloys (SMAs) were investigated. The sequence of the phase formation and transformations in dependence on the chemical composition is established. Rapidly solidified Ti-Ni-Hf or Ti-Ni-Si SMAs are found to show relatively high yield strength and large ductility for specific Hf or Si concentrations, which is due to the gradual disappearance of the phase transformation from austenite to twinned martensite and the predominance of the phase transformation from twinned martensite to detwinned martensite during deformation as well as to the refinement of dendrites and the precipitation of brittle intermetallic compounds.

Keywords martensitic phase transformation, mechanical properties, microstructures, rapid solidification

1. Introduction

In recent years, many investigations have been focused on TiNi-based shape memory alloys (SMAs) due to their extraordinary shape memory effect, superelasticity, good biocompatibility, and ductility (Ref 1-5). Up to now, TiNi-based SMAs have been considered as one of the most candidates for potential applications (Ref 1-4). By introducing a third element such as Fe, Al, Hf, Cu, or Zr into nearly equiatomic Ti-Ni binary alloys, martensitic transformation (MT) and the shape memory effect (SME) can be effectively improved together with adjusting the phase formation process (Ref 1-4, 6-18). For example, the MT sequence in Ti-Ni binary alloys is $B2 \rightarrow B19'$, while it changes to be $B2 \rightarrow R \rightarrow B19'$ in Ti-Ni-Fe and Ti-Ni-Al alloys or $B2 \rightarrow B19 \rightarrow B19'$ in Ti-Ni-Cu alloys (Ref 6-12). Furthermore, the MT sequence in Ti-Ni alloys can also be changed to $B2 \rightarrow R \rightarrow B19'$ after thermal cycle training, heat treatment after cold working, or aging treatment in Ni-rich Ti-Ni alloys (Ref 3, 5, 6, 13). As a result, the MT temperatures can be effectively tailored based on the industrial

requirements in different TiNi-based SMAs (Ref 14-18), which further promotes their widespread practical applications.

However, the yield strength of TiNi-based SMAs is relatively low compared with other metallic materials such as some Fe-based SMA alloys, even though their fracture strength is quite high (Ref 5). Until now, a variety of methods have been proposed to enhance the mechanical properties in the premise of remaining their excellent shape memory effect (SME), e.g., (1) by introducing micro-alloying elements in order to induce the precipitation of other intermetallic compounds, (2) by thermal cycling training, (3) by cold-working, (4) by aging (Ref 3, 5, 19). It has been demonstrated that the microstructures of metallic alloys tend to become finer after rapid solidification (Ref 20, 21), which is useful for the enhancement of mechanical properties. Therefore, it could be a good choice to modify the grain size by adopting rapid solidification together with considering compositional optimization. This is a subject of the present work, in which TiNi-based SMAs with additions either Hf or Si were prepared by rapid solidification and the compositional dependence of microstructural features, MT behaviors, and mechanical properties was systematically investigated.

2. Experimental Procedure

$\text{Ti}_{50-x/2}\text{Ni}_{50-x/2}\text{Hf}_x$ ($x = 0, 2, 4, 6, 8, 10,$ and 12 at.%) and $\text{Ti}_{50-y/2}\text{Ni}_{50-y/2}\text{Si}_y$ ($y = 1, 2, 3, 5, 7,$ and 10 at.%) master alloys were prepared by arc-melting appropriate amounts of the constituting elements ($> 99.9\%$ purity) under Ti-gettered Ar atmosphere. The master alloys were remelted at least four times in order to achieve chemical homogeneity. Subsequently, rods with a diameter of approximately 1.5 mm and a length of 80 mm were fabricated using a custom-made suction-casting device under Ar atmosphere. Phase analysis of the as-cast samples was carried out using x-ray diffraction (XRD, Rigaku D/max-rB) in reflection geometry and scanning electron microscopy (SEM, Gemini 1530) combined with energy-dispersive x-ray spectroscopy (EDS). The MT behavior was

X.L. Han, K.K. Song, and L. Wang, School of Mechanical, Electrical and Information Engineering, Shandong University (Weihai), Weihai 264209, People's Republic of China; L.M. Zhang and H. Xing, Department of Applied Physics, Northwestern Polytechnical University, Xi'an 710072, People's Republic of China; B. Sarac, Erich Schmid Institute of Materials Science, Austrian Academy of Sciences, 8700 Leoben, Austria; F. Spieckermann, T. Maity, and M. Mühlbacher, Department Materials Physics, Montanuniversität Leoben, 8700 Leoben, Austria; and I. Kaban, IFW Dresden, Institute for Complex Materials, Helmholtzstr. 20, 01069 Dresden, Germany; and J. Eckert, Erich Schmid Institute of Materials Science, Austrian Academy of Sciences, 8700 Leoben, Austria; and Department Materials Physics, Montanuniversität Leoben, 8700 Leoben, Austria. Contact e-mail: songkaikai8297@gmail.com.

determined through differential scanning calorimetry (DSC) at a heating and cooling rate of 20 K/min for four times. Room-temperature compression experiments were carried out with a universal testing machine (CMT 5305, New SANS, MTS). The surface features of the samples unloaded under different compressive strains were also checked by the SEM.

3. Results and Discussion

3.1 Phase Analysis of the Rapidly Solidified Ti-Ni-Hf and Ti-Ni-Si Samples

Figure 1 shows the XRD patterns of the rapidly solidified Ti-Ni-Hf and Ti-Ni-Si rods with a diameter of 1.5 mm, respectively. Although the diffraction peaks are rather wide, no glass transition has been detected on the DSC curves (not shown here), implying no any amorphous phase can be induced during rapid solidification. From positions of the Bragg peaks (Fig. 1a), the crystals in the present rapidly solidified Ti-Ni-Hf rods can be indexed to be cubic B2 ($Pm-3m$) TiNi austenitic phase and monoclinic B19' ($P2_1/m$) TiNi martensites together with a little amount of Ti_2Ni phase. With increasing Hf content, the amount of B2 TiNi crystals gradually decreases while that of B19' ($P2_1/m$) TiNi martensites increases. B2 TiNi is a dominant crystalline phase for Hf additions of less than 4 at.%, while the B19' TiNi crystals start to be prevalent for the larger Hf amount. Gupta et al. found that a continuous series of solid solutions exists between the HfNi and NiTi phases at the high temperatures (> 1448 K) (Ref 22), implying that Hf tends to be dissolved into TiNi and Ti_2Ni crystals. As a result, the positions of the Bragg diffraction peaks shift to the left side in the XRD patterns (see the dotted line in Fig. 1a) (Ref 22), leading to the formation of B2 (Ti,Hf)Ni, B19' (Ti,Hf)Ni, and a small amount of $(Ti,Hf)_2Ni$. On the other hand, for the present rapidly solidified Ti-Ni-Si rods (Fig. 1b), the microstructures are governed by B2 TiNi crystals together with a minor amount of B19' TiNi crystals when the content Si is below 5 at.%. With increasing Si content (≤ 5 at.%), the content of B2 gradually increases and then decreases. With further increasing Si content (> 5 at.%), B19' TiNi and $Ti_4Ni_4Si_7$ crystals become prevalent, while the content of B2 TiNi crystals becomes gradually lower (Fig. 1b). Since the solid solubility of Si in TiNi crystals is relatively small, the positions of the diffraction peaks do not change (see the dotted line in Fig. 1b).

The morphologies of the crystals in the rapidly solidified Ti-Ni-Hf and Ti-Ni-Si rods are displayed in Fig. 2 and 3, respectively. (Only selected images are shown for clarity.) For the rapidly solidified $Ti_{50}Ni_{50}$ binary alloy, the B2 TiNi and B19' TiNi martensitic crystals exhibit a cellular dendritic feature, while not obvious other intermetallic compounds precipitate in the matrix (Fig. 2a). When the content of Hf changes from 2 to 12 at.%, the cellular dendrites gradually become finer and develop into dendrites (Fig. 2). With increasing Hf content in the alloys, Ti_2Ni intermetallic phase appears in the interdendritic regions. The compositions of the present alloys are still far away from eutectic compositions, and a large degree of undercooling should be induced during rapid solidification, leading to the formation and development of primary TiNi dendrites (see regions A and B whose compositions are listed in Table 1) followed by intercrystalline segregation of $(Ti,Hf)_2Ni$ crystals (see region C in Fig. 2). As

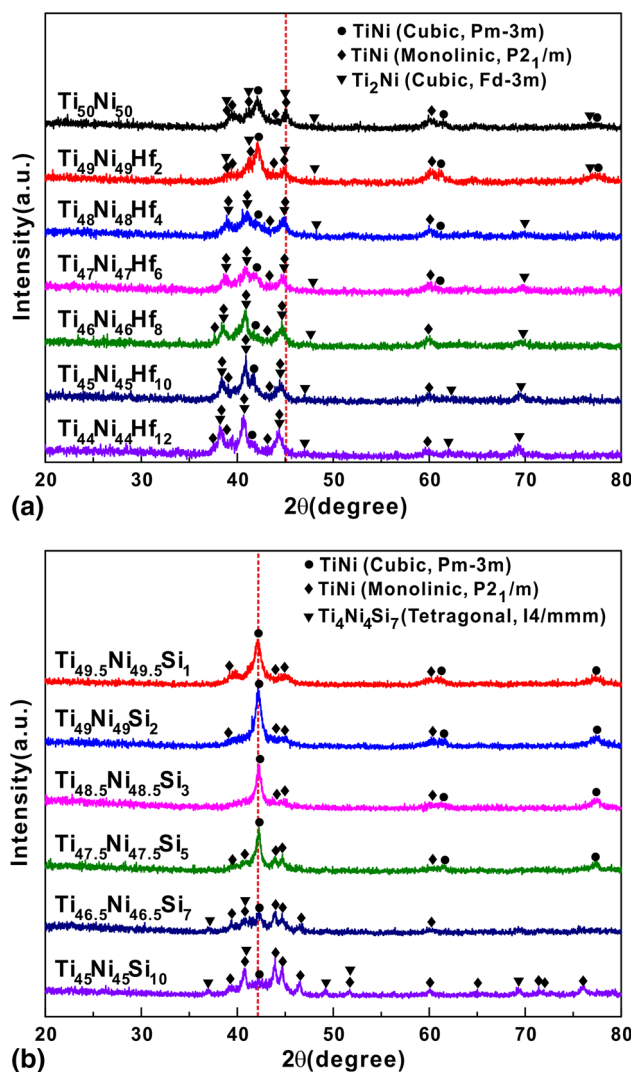


Fig. 1 XRD patterns of the rapidly solidified (a) Ti-Ni-Hf and (b) Ti-Ni-Si samples

listed in Table 1, the corresponding compositions were determined to be $(Ti,Hf)_2Ni$ by EDS, whose amount gradually increases when the Hf content increases from 0 to 12 at.%. Besides, some TiNi martensitic plates can be observed within the dendrites (Fig. 2c, f), whose content gradually increases with increasing amount of Hf.

For the rapidly solidified Ti-Ni-Si samples with the addition of less than 3 at.% Si, the dominant crystals are still TiNi cellular dendrites (Fig. 3a). With further increasing Si content, the cellular dendrites gradually become finer and develop dendrites in the present Ti-Ni-Si alloys (region A in Fig. 3), whose corresponding compositions are listed in Table 1. When the content of Si is more than 5 at.%, some $Ti_4Ni_4Si_7$ crystals start to precipitate at the interdendritic regions (see the region C in Fig. 3b-d) since the extra Si cannot be dissolved in the TiNi crystals. As shown in Fig. 3(e), (f), and (g), EDS maps clearly reveal that the distribution of Si in the rapidly solidified Ti-Ni-Si alloys is not uniform, but Si mainly exists at the interdendritic regions. As a result, the eutectic structure consisting of some TiNi and $Ti_4Ni_4Si_7$ crystals forms (see the inset in Fig. 3c). The compositions of the different phases were determined by EDS and are listed in Table 1.

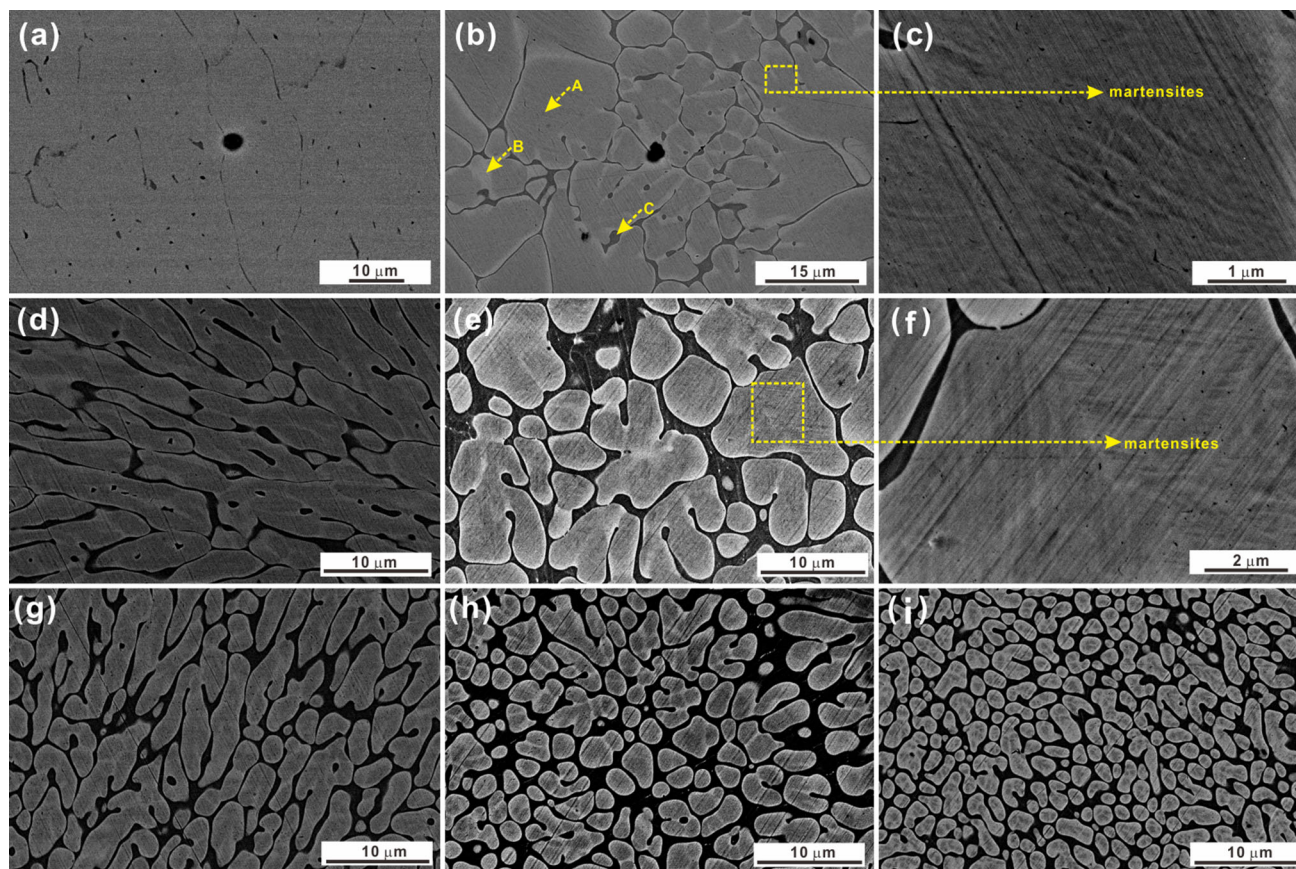


Fig. 2 SEM images of the rapidly solidified (a) $\text{Ti}_{50}\text{Ni}_{50}$, (b, c) $\text{Ti}_{49}\text{Ni}_{49}\text{Hf}_2$, (d) $\text{Ti}_{48}\text{Ni}_{48}\text{Hf}_4$, and (e, f) $\text{Ti}_{47}\text{Ni}_{47}\text{Hf}_6$, (g) $\text{Ti}_{46}\text{Ni}_{46}\text{Hf}_8$, (h) $\text{Ti}_{45}\text{Ni}_{45}\text{Hf}_{10}$, (i) $\text{Ti}_{44}\text{Ni}_{44}\text{Hf}_{12}$ samples

3.2 Martensitic Transformations in Rapidly Solidified Ti-Ni-Hf and Ti-Ni-Si Alloys

In order to investigate the MT behavior of the rapidly solidified Ti-Ni-Hf and Ti-Ni-Si samples, low-temperature DSC measurements were taken (Fig. 4). As shown in Fig. 4(a) for the Ti-Ni-Hf alloys, a two-stage phase transformation can be observed when the content of Hf is less than 4 at.%. When the content of Hf is between 4 and 8 at.%, the two-stage phase transformation seems to change to a one-stage process. With the addition of 10 or 12 at.% Hf, the two-stage phase transformation behavior becomes obvious again. In contrast, all investigated rapidly solidified Ti-Ni-Si samples Fig. 4(b) exhibit a two-stage phase transformation behavior even though it becomes weak with the addition of 3 at.% Si. Generally speaking, TiNi-based alloys experience a one-stage MT, and a multistage phase transformation can only be observed by adjusting alloy compositions or after special heat or mechanical treatment (Ref 14, 16, 19, 23-25). It has been shown that the two-stage phase transformation paths can be classified into (1) $\text{B2} \rightarrow \text{R} \rightarrow \text{B19}'$ in some Ti-Ni-Fe alloys or aged Ti-Ni alloys when equiatomic TiNi is subjected to thermal cycling or cold working, and (2) $\text{B2} \rightarrow \text{B19} \rightarrow \text{B19}'$ in some Ti-Ni-Cu alloys (Ref 23, 24). After aging, solution treatment, or thermal cycling Ti-Ni-Hf alloys usually show a one-stage phase transformation path, which can be attributed to the $\text{B2} \rightarrow \text{B19}'$ transformation (Ref 14, 16, 19, 25). This finding is incompatible with our investigations on Ti-Ni-Hf alloys. Nagarajan et al. have shown that nanoscale T_2Ni particles prefer to precipitate

in the TiNi intermetallic matrix for rapidly solidified equiatomic TiNi alloys (Ref 26). Moreover, Nam et al. also found that rapid solidification can induce a large amount of crystallographic defects such as dislocations, which strongly depends on the applied cooling rates (Ref 24, 27). As a result, a two-stage phase transformation path appears in TiNi-based SMAs (Ref 6, 18). In our case, Hf possesses a similar electronic configuration in the outer shells as Ti, i.e., has a d^2 configuration. Thus, it is expected that Hf tends to substitute Ti, leading to the gradual precipitation of $(\text{Ti,Hf})_2\text{Ni}$ crystals. As shown in Fig. 1(a) and 2, the amount of $(\text{Ti,Hf})_2\text{Ni}$ precipitates indeed gradually increases with increasing Hf content, which can lead to variations in chemical composition and internal stresses in the TiNi matrix (Ref 28, 29) close to and far from $(\text{Ti,Hf})_2\text{Ni}$ precipitates. In fact, the dendrites consisting of B2 TiNi and/or B19' TiNi crystals display a dark region inside dendrites (region A in Fig. 2) and a gray region at the edges of dendrites (region B in Fig. 2) for the present Ti-Ni-Hf specimens but not for the binary $\text{Ti}_{50}\text{Ni}_{50}$ sample. As shown in Table 1, the compositions of both regions, which are associated with B2 TiNi and/or B19' TiNi phases, are Ni rich and the ratio of Ti and Ni is almost constant. However, there is still a small compositional difference between these two regions, especially concerning the Hf content. Previous reports have shown that even a small compositional difference can induce a change in the martensitic transformation (Ref 1, 4, 30). Therefore, in our case, the variations in the chemical compositions and internal stresses in the TiNi matrix close to and far from the Ti_2Ni precipitates could be the main reasons for the appearance of the

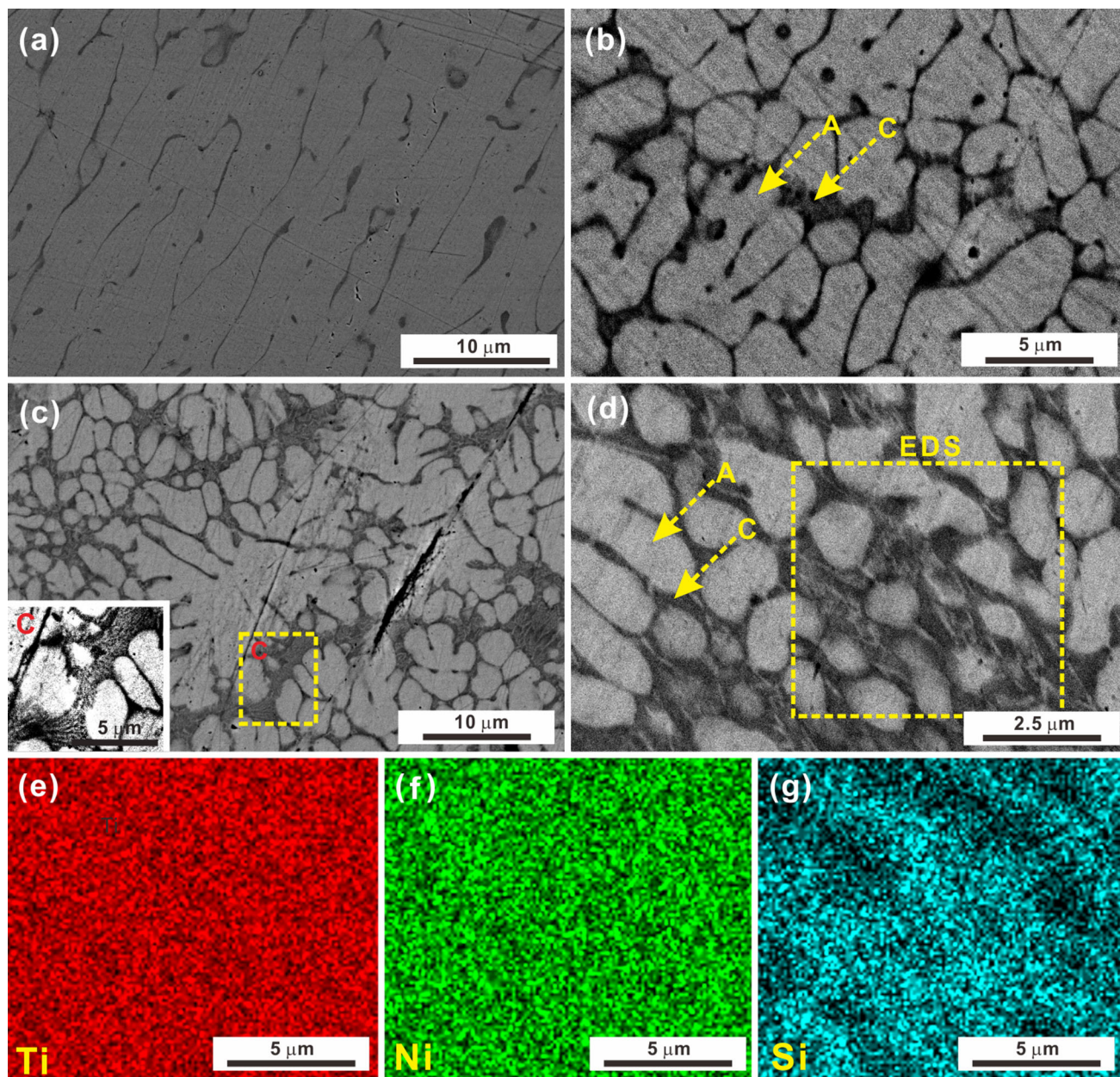


Fig. 3 SEM images of the rapidly solidified (a) $\text{Ti}_{49}\text{Ni}_{49}\text{Si}_2$, (b) $\text{Ti}_{48.5}\text{Ni}_{48.5}\text{Si}_3$, (c) $\text{Ti}_{47.5}\text{Ni}_{47.5}\text{Hf}_5$, and (d) $\text{Ti}_{46.5}\text{Ni}_{46.5}\text{Si}_7$ samples (inset: local enlarged image of eutectic structures); distribution of elements (e) Ti, (f) Ni, (g) Si in the as-quenched $\text{Ti}_{46.5}\text{Ni}_{46.5}\text{Si}_7$ samples

Table 1 Compositions of different regions in the as-cast Ti-Ni-Hf and Ti-Ni-Si samples

Compositions	Different regions	Ti (at.%)	Ni (at.%)	Hf or Si (at.%)	Crystalline phases
$\text{Ti}_{49}\text{Ni}_{49}\text{Hf}_2$	A phase	44.5 ± 1	53.2 ± 1	2.3 ± 1.5	TiNi
	B phase	44.9 ± 1	53.3 ± 1	1.8 ± 1.5	TiNi
	C phase	60.1 ± 1	37.6 ± 1	2.3 ± 1.5	Ti_2Ni
$\text{Ti}_{45}\text{Ni}_{45}\text{Hf}_{10}$	A phase	36.9 ± 1	52.5 ± 1	10.6 ± 1.5	TiNi
	B phase	38.2 ± 1	51.7 ± 1	10.1 ± 1.5	TiNi
	C phase	52.6 ± 1	37.8 ± 1	9.6 ± 1.5	Ti_2Ni
$\text{Ti}_{48.5}\text{Ni}_{48.5}\text{Si}_3$	A phase	49.0 ± 1	48.2 ± 1	2.8 ± 1.5	TiNi
	C phase	44.7 ± 1	45.3 ± 1	10.0 ± 1.5	TiNi + $\text{Ti}_4\text{Ni}_4\text{Si}_7$
$\text{Ti}_{46.5}\text{Ni}_{46.5}\text{Si}_7$	A phase	49.3 ± 1	47.6 ± 1	3.1 ± 1.5	TiNi
	C phase	45.0 ± 1	44.8 ± 1	10.2 ± 1.5	TiNi + $\text{Ti}_4\text{Ni}_4\text{Si}_7$

two-stage phase transformation path. Only when the content of Hf is between 4 and 8 at.%, the TiNi austenites gradually transform into martensites, which can effectively release the internal stresses in the TiNi matrix, resulting in the disappearance and/or the fuzziness of the two-stage phase transformation path. Such a change in the phase transformation path seems to appear also in the present rapidly solidified Ti-Ni-Si alloys (Fig. 4b) even though the precipitates in the matrix are $\text{Ti}_4\text{Ni}_4\text{Si}_7$ intermetallic compounds but not Ti_2Ni phase. However, as shown in Fig. 3(a), the dendrites consisting of B2 TiNi and/or B19' TiNi crystals do not obviously display both a dark region inside dendrites and a gray region at the edges of dendrites for the present Ti-Ni-Si samples. In fact, the gray regions mentioned for the Ti-Ni-Hf alloys appear in the interdendritic regions (see Fig. 3d) together with dark $\text{Ti}_4\text{Ni}_4\text{Si}_7$ intermetallic compounds (Fig. 3c) suggesting the formation of a eutectic structure in these alloys. When the content of Si gradually increases, this eutectic structure becomes more obvious (Fig. 3), further corroborating the enhancement of the variations in the chemical compositions and internal stresses in the present Ti-Ni-Si alloys (Fig. 3e, f, and g). Hence, a two-stage phase transformation paths also can be observed during thermal cycling.

Usually, TiNi-based alloys undergo cyclic phase transformation between B2 structured austenite and B19' structured martensite during service. Therefore, the stability of the phase transformation behavior during cycling is of crucial practical importance. As shown in Fig. 5(a), with increasing number of thermal cycles the M_s temperature decreases slightly with the addition of a small amount of Hf and then rises with further increasing Hf content for the rapidly solidified Ti-Ni-Hf alloys. For the rapidly solidified Ti-Ni-Si alloys (Fig. 5b), the M_s temperature also decreases upon thermal cycling when the Si content is below 3 at.%. When the content of Si exceeds 3 at.%, the M_s temperature remains almost constant. It has been proposed that thermal cycling of SMAs can induce the generation of a large density of dislocations and distinct dislocation substructures (Ref 31-33). Dislocations are lattice defects which can help to accommodate elastic stresses associated with the formation of martensites, but they can also act as obstacles (Ref 34, 35). Then dislocation-triggered plasticity renders martensites difficult to form, leading to the decrease in M_s temperature (Ref 31, 36). On the other hand, the critical stress required to form stress-induced martensite decreases due to the appearance of dislocation reactions, which promote the MT (Ref 37, 38). When no substantial change in

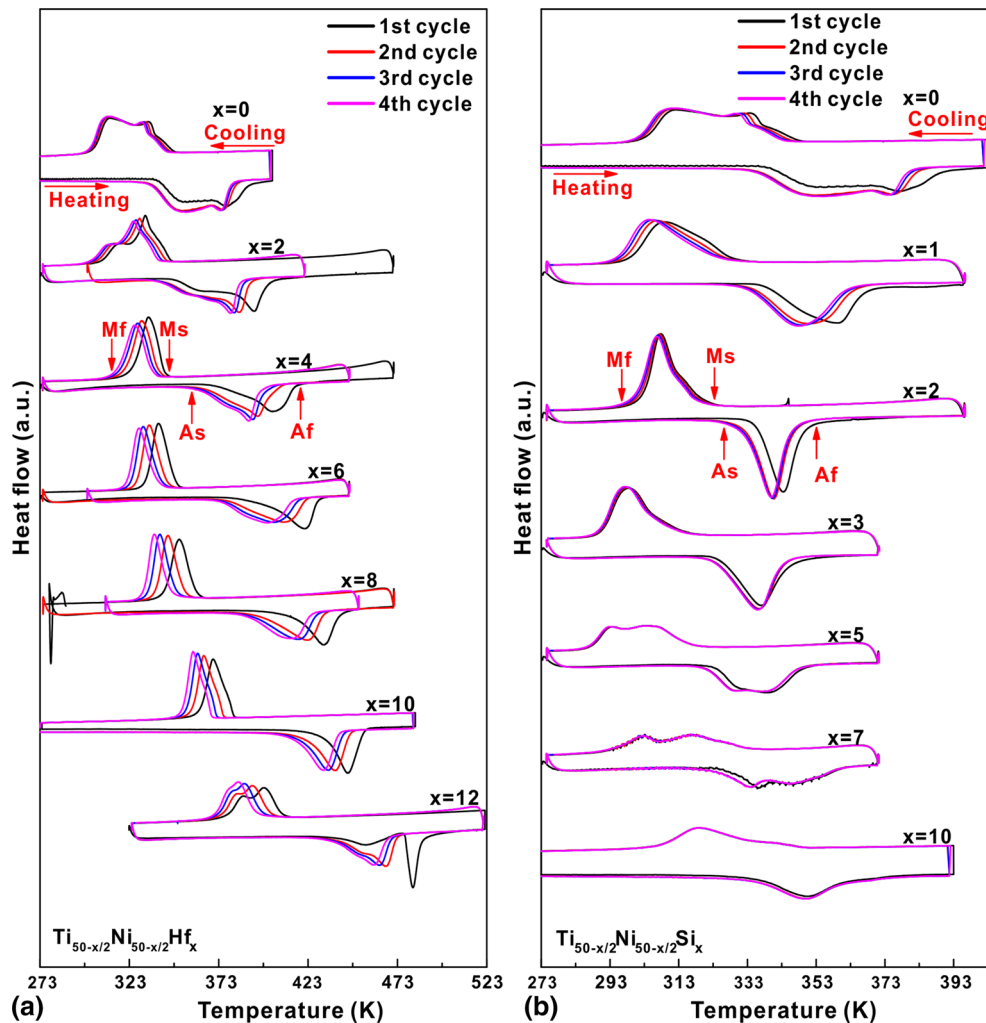


Fig. 4 Low-temperature DSC curves (heating and cooling rate 20 K/min) of the rapidly solidified (a) Ti-Ni-Hf and (b) Ti-Ni-Si alloys under different thermal training cycles

the microstructure occurs upon thermal cycling, then the M_s temperature can remain constant. It can be expected from our results that the addition of micro-alloying elements such as Hf and Si strongly affects the formation of dislocations in SMAs, leading to a different thermal cycling dependence of the M_s temperature in equiatomic TiNi-based SMAs.

In order to clarify the role of Hf or Si addition on the M_s temperature, the phase transformation temperatures derived in the present study together with data for reference alloys (Ref 25, 39-43) are plotted in Fig. 6. In general, it can be seen that the transformation temperatures of the present Ti-Ni-Hf alloys exhibit a rising trend with increasing Hf content (Fig. 6a). However, the phase transformation temperatures of the investigated Ti-Ni-Si alloys decrease first and then increase again (Fig. 6b). Until now, several parameters have been proposed to evaluate the tendency and changes in the phase transformation temperatures in SMAs based on the average concentration of valence electrons (Ref 44, 45), among which the valence electrons-per-atom ratio, e_v/a , of ternary and quaternary alloys is one of the most effective parameters (Ref 44, 45) which can be calculated by the following equation:

$$\frac{e_v}{a} = f^A e_v^A + f^B e_v^B + f^C e_v^C, \quad (\text{Eq 1})$$

where f^A , f^B , and f^C are the atomic fractions of the different elements (A, B, and C) and e_v^A , e_v^B , and e_v^C are the number of valence electrons of the different constituent elements. The values of e_v/a remain constant ($= 7.5$) for some SMAs, which implies that other factors should be also considered (Ref 44, 45). The compositional dependence of the phase transformation temperatures of SMAs is suggested to be linked to the variation of the average concentration of valence electrons (c_v) of an alloy. The c_v value of an alloy can be calculated by the ratio of the number of valence electrons to the total number of electrons of the alloy, $c_v = e_v/e_t$, and is given by (Ref 44, 45):

$$c_v = \frac{e_v}{e_t} = \frac{f^A e_v^A + f^B e_v^B + f^C e_v^C}{f^A N^A + f^B N^B + f^C N^C}, \quad (\text{Eq 2})$$

where N^A , N^B , and N^C are the atomic numbers of the elements in the alloy, respectively. Table 2 lists the values of e_v/a and c_v of the present Ti-Ni-Hf and Ti-Ni-Si alloys. It can be seen that the phase transformation temperature shifts to higher temperatures with decreasing values of e_v/a and c_v when the content of Hf lies between 0 and 12 at.% or the content of Si is between 0 and 3 at.%. It has been demonstrated that the decrease in both e_v/a and c_v implies a decrease in the number of valence electrons and/or an increase in the atomic volume of the alloy due to a higher number of non-valence electrons (Ref 44-46), leading to a reduction in the valence electron densities in both austenite and martensite. Generally speaking, a lower valence electron density results in a lower bulk and shear modulus of an alloy (Ref 46, 47). In other words, the decrease in the valence electron density of TiNi-based SMAs is expected to result in lower elastic and shear moduli. Since the elastic moduli decrease during cooling and reach a critical value before MT (Ref 3, 44, 45), the critical elastic constant can be reached at higher temperatures, leading to the increase in the M_s temperature. However, when the Si content exceeds 3 at.%, the phase transformation temperature gradually increases with both increasing e_v/a and c_v , which is contrary with the observations described above. Recently, Marchezini et al. have proven that the strategy to evaluate the stability of an alloy with respect to MT by considering e_v/a or c_v does not account for the influence of microstructural features such as grain sizes, secondary phases, ordering, and defect concentration (Ref 48). In our case, the grain sizes of both TiNi-based alloy systems are gradually reduced with the addition of Hf and Si. However, the M_s of the present Ti-Ni-Hf alloys do not display a monotone change tendency with grain size reducing, implying that the decrease in grain size should be not responsible for it. It is worth noting that when the Si content is more than 3 at.%, some $\text{Ti}_4\text{Ni}_4\text{Si}_7$ intermetallics start to precipitate at the interdendritic regions as one component of the eutectic microstructure, which could be the main reason for the increase in the phase transformation temperature for the samples with higher Si additions.

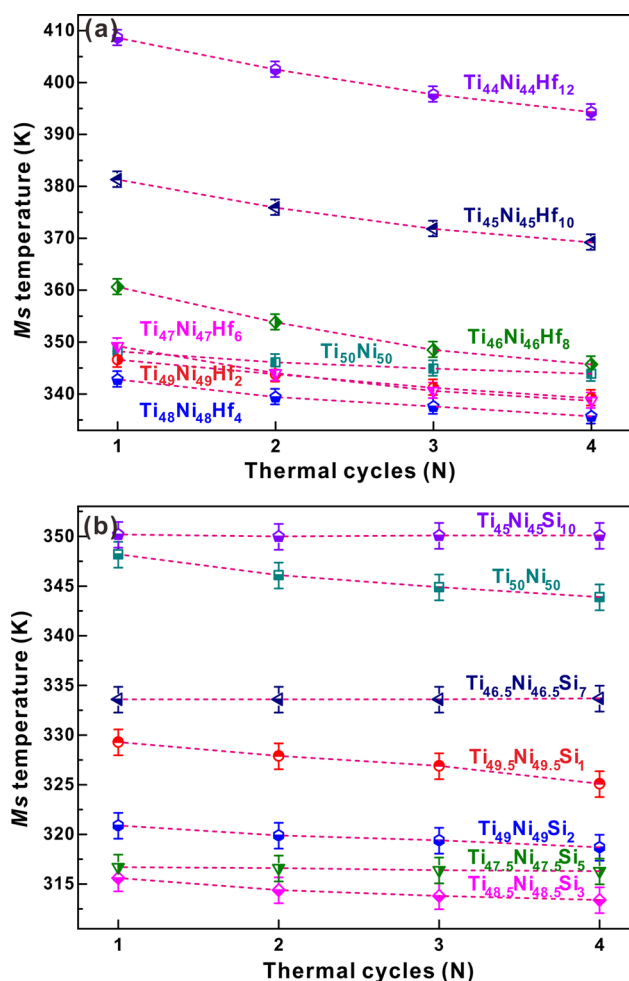


Fig. 5 Dependence of the M_s temperature on the thermal cycles for the rapidly solidified (a) Ti-Ni-Hf and (b) Ti-Ni-Si samples

3.3 Mechanical Properties of the Rapidly Solidified Ti-Ni-Hf and Ti-Ni-Si Samples

In order to check the mechanical performance of the present rapidly solidified Ti-Ni-Hf and Ti-Ni-Si alloys, room-temper-

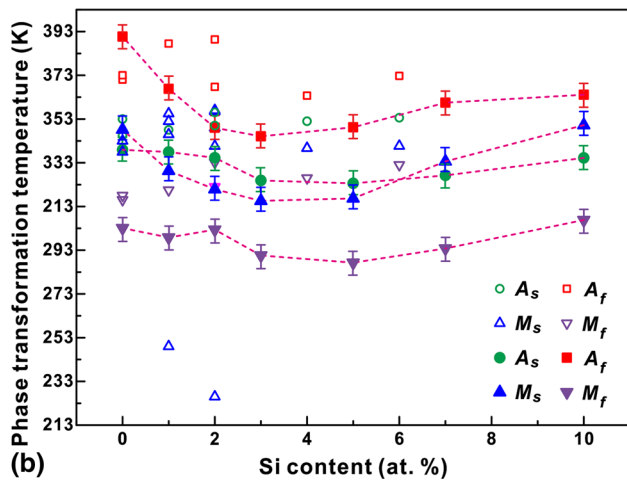
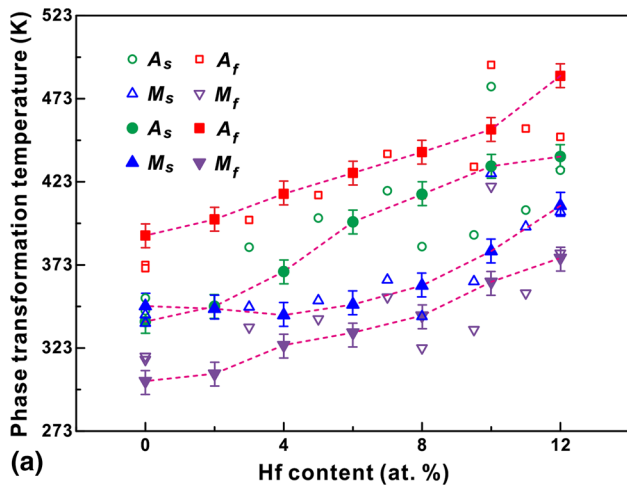


Fig. 6 Effect of Hf content on the phase transformation temperatures of the rapidly solidified $Ti_{50-x/2}Ni_{50-x/2}Hf_x$ ($x = 0, 2, 4, 6, 8, 10,$ and 12 at.%) and effect of Si content on the phase transformation temperatures of the as-cast $Ti_{50-y/2}Ni_{50-y/2}Si_y$ ($y = 1, 2, 3, 5, 7,$ and 10 at.%) samples. The data marked by the solid symbols were obtained in this study; data from previous reports were labeled as hollow symbols (Ref 25, 39-43)

Table 2 Values of e_v/a and c_v of the investigated Ti-Ni-Hf and Ti-Ni-Si samples, respectively

Compositions	e_v/a	c_v
$Ti_{50}Ni_{50}$	7	0.28
$Ti_{49}Ni_{49}Hf_2$	6.94	0.26754
$Ti_{48}Ni_{48}Hf_4$	6.88	0.25595
$Ti_{47}Ni_{47}Hf_6$	6.82	0.24515
$Ti_{46}Ni_{46}Hf_8$	6.76	0.23505
$Ti_{45}Ni_{45}Hf_{10}$	6.7	0.22559
$Ti_{44}Ni_{44}Hf_{12}$	6.64	0.21671
$Ti_{49.5}Ni_{49.5}Si_1$	7.07	0.28405
$Ti_{49}Ni_{49}Si_2$	7.14	0.28814
$Ti_{48.5}Ni_{48.5}Si_3$	7.21	0.29226
$Ti_{47.5}Ni_{47.5}Si_5$	7.35	0.30061
$Ti_{46.5}Ni_{46.5}Si_7$	7.49	0.30912
$Ti_{45}Ni_{45}Si_{10}$	7.7	0.32218

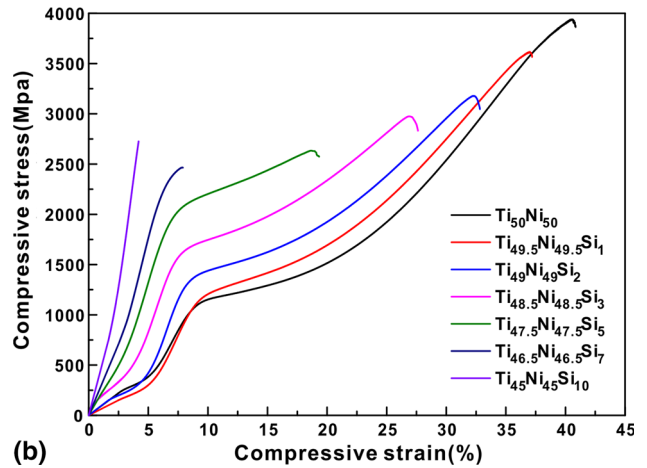
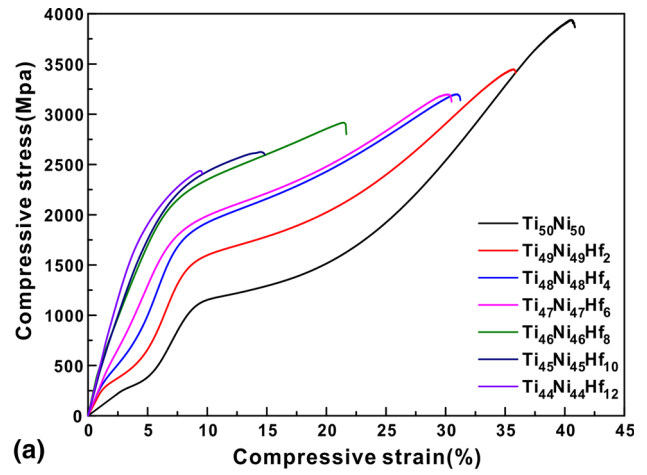


Fig. 7 Compressive stress-strain curves of the rapidly solidified (a) Ti-Ni-Hf and (b) Ti-Ni-Si samples

ure compression experiments were performed. As shown in Fig. 7(a), the yield strength of the rapidly solidified Ti-Ni-Hf alloys raises from 277 ± 5 to 1370 ± 5 MPa while their fracture strength and plastic strain drop from 3880 ± 10 MPa and $37.5 \pm 1\%$ to 2407 ± 10 MPa and $6.5 \pm 1\%$ with increasing Hf content, respectively. According to the XRD and SEM results, the dominant phase in the rapidly solidified TiNi-based alloys containing a low amount of Hf is B2 TiNi austenite. During deformation, the B2 TiNi austenite gradually transforms to martensite after experiencing the elastic region (Fig. 8a). With increasing applied stress, a large amount of twinned martensite appears within the B2 TiNi austenite and the compressive deformation curves enter a first plateau (marked by the arrows in Fig. 7a). Afterward, the twinned martensite starts to be deformed elastically and then yields due to detwinning (Fig. 8b). It has been demonstrated that a resolved shear stress acts on the twin planes of the twinned martensite during deformation and drives the twin boundary to move apart when it reaches a critical value by the formation and movement of a high density of dislocations (Ref 30). At the same time, a large number of slip bands appear around the grain boundaries and gradually develop into micro-cracks with increasing applied stress until failure (Fig. 8c and d). However, when the content of Hf further increases, the yield strength before the first plateau is enhanced while the plastic strain corresponding to the first plateau decreases due to the decrease in the ratio of austenite

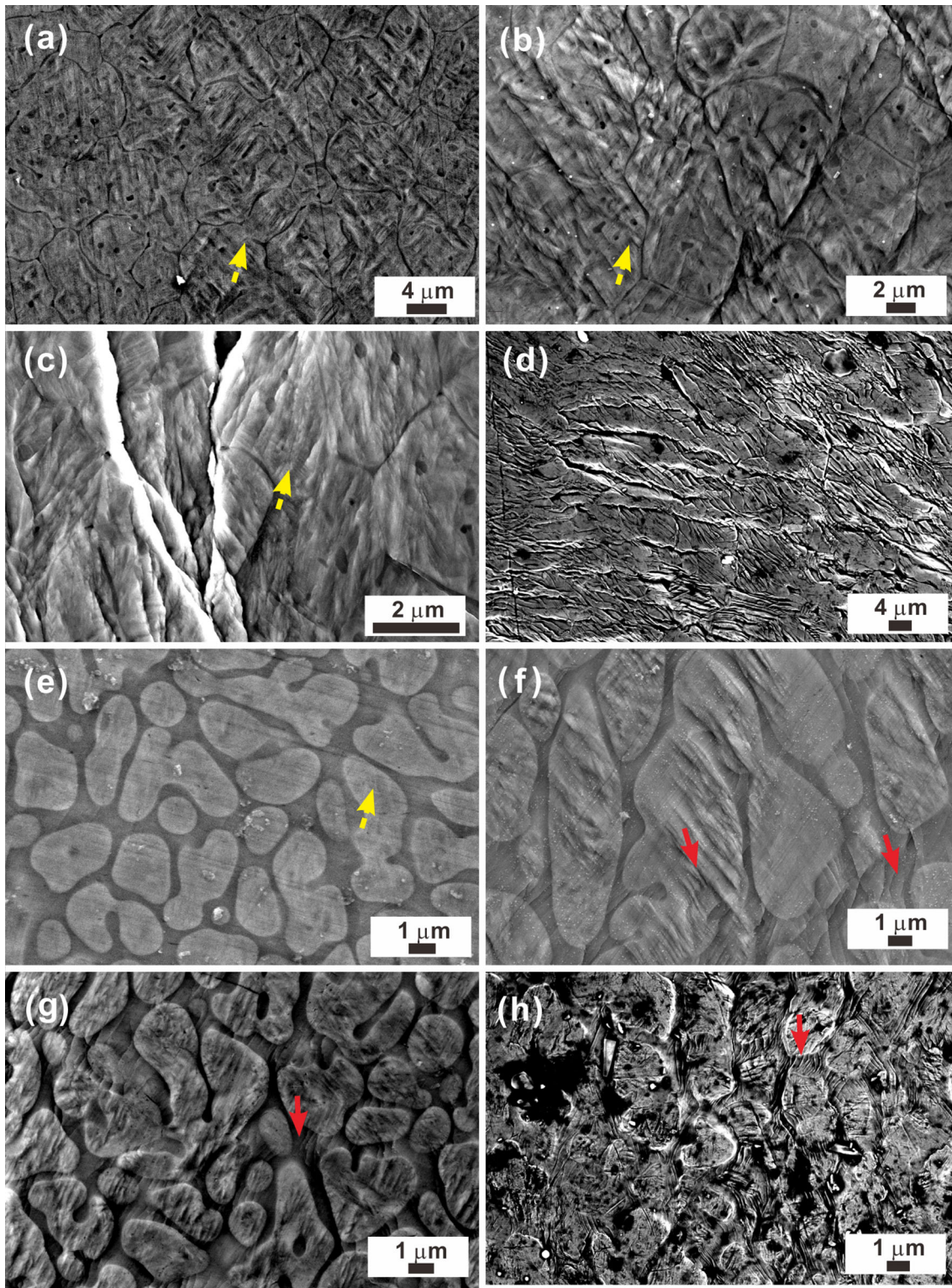


Fig. 8 SEM images of the as-cast samples unloaded at different compressive strains, i.e., (a) 2.2%, (b) 11.3%, (c) 33.6%, and (d) after fracture for the as-cast $\text{Ti}_{49}\text{Ni}_{49}\text{Hf}_2$ samples; (e) 2.3%, (f) 6.8%, (g) 11.0%, and (h) after fracture for the as-cast $\text{Ti}_{45}\text{Ni}_{45}\text{Hf}_{10}$ samples

and martensite (Fig. 7a). Besides, brittle Ti_2Ni precipitates can also strengthen the alloys and increase the critical stress for plastic deformation. However, when the content of Hf is higher than 6 at.%, the dominant crystals are not TiNi austenite but TiNi martensite, resulting in the gradual disappearance of the first plastic plateau. Then, the plastic deformation is strongly

governed by the deformation of twinned TiNi martensite but not by B2 TiNi crystals (Ref 3, 49). As shown in Fig. 8(e), no obvious microstructural changes can be observed compared with the as-quenched samples, leading to a higher yield strength. With increasing stress, some fine slip bands start to appear around the interfaces around and within the TiNi

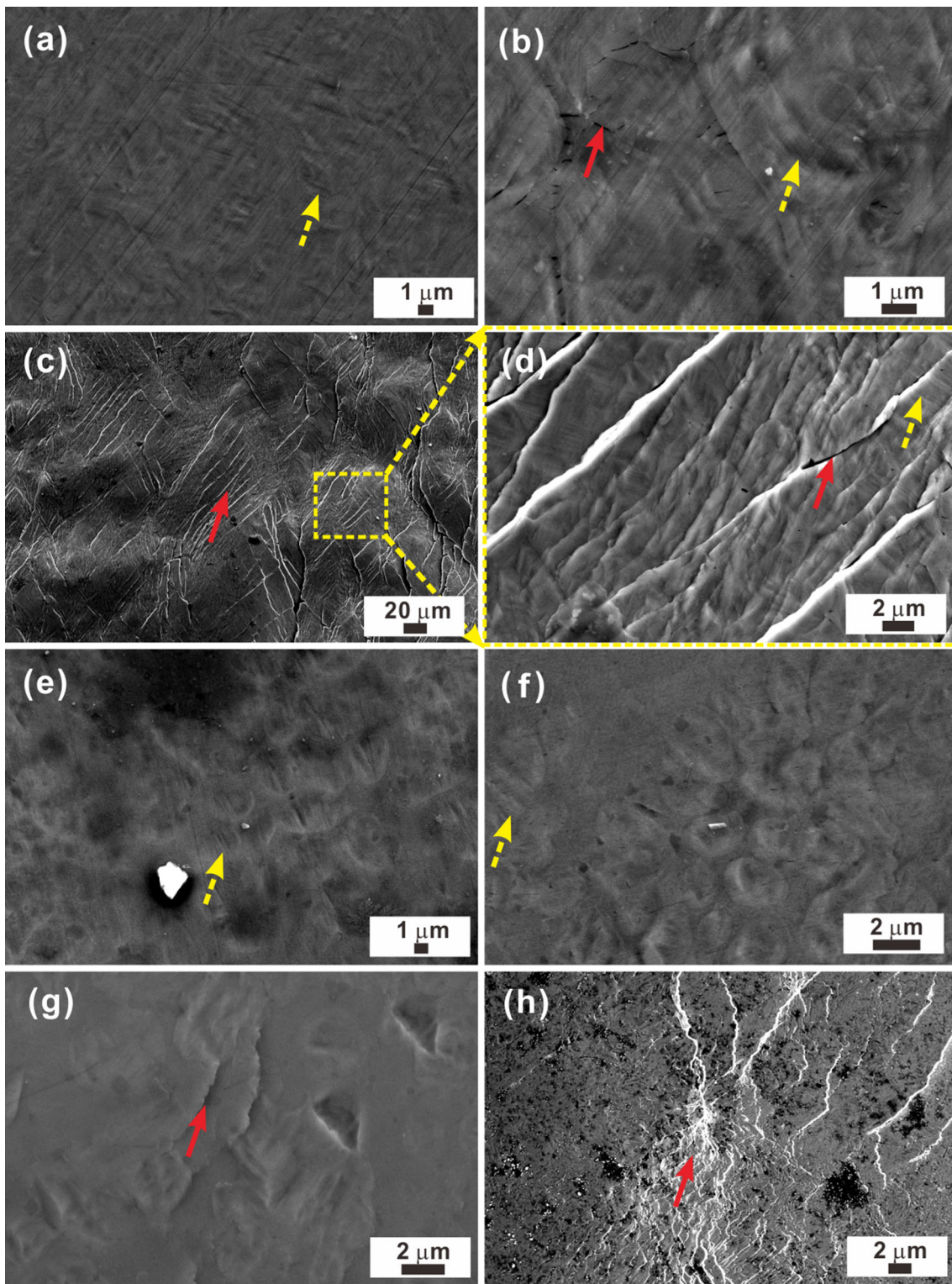


Fig. 9 SEM images of the as-cast samples unloaded at different compressive strains, i.e., (a) 1.8%, (b) 10.1%, (c) 32.1%, and (d) after fracture for the as-cast $\text{Ti}_{49}\text{Ni}_{49}\text{Si}_2$ samples; (e) 1.3%, (f) 3.6%, (g) 5.8%, and (h) after fracture for the as-cast $\text{Ti}_{46.5}\text{Ni}_{46.5}\text{Si}_7$ samples

martensite (Fig. 8f), respectively. These microstructural changes gradually become more and more pronounced (Fig. 8g) and finally evolve into micro-cracks, leading to the failure of the samples (Fig. 8h).

For the rapidly solidified Ti-Ni-Si alloys (Fig. 7b), their yield strength decreases from 277 ± 5 to 173 ± 5 MPa and then

gradually increases to 970 ± 20 MPa when the Si content increases from 0 to 3 at.% and then further to 10 at.%. When the Si content is larger than 3 at.%, the yield strength gradually increases while both the failure strength and the plastic strain decrease from 3880 ± 10 MPa and $37.5 \pm 1\%$ to 2467 ± 10 MPa and $5 \pm 1\%$, respectively, when the Si content

increases to 7 at.%. When the Si content reaches 10 at.%, the fracture strength is 2731 ± 10 MPa and the plastic strain is about 2%. As shown in Fig. 1 and 3, the contents of B2 TiNi austenite and TiNi martensite gradually increase and decrease, respectively, with increasing Si content from 0 to 3 at.%. Therefore, the samples with less than 3 at.% exhibit some martensitic crystals within the TiNi austenite after experiencing the elastic region (Fig. 9a). With increasing applied stress or strain (i.e., unloaded at a strain of 10.1%), some fine micro-cracks and slip bands appear around the dendrites together with a larger amount of stress-induced martensite (Fig. 9b). When the applied stress increases to 32.1%, a large amount of slip bands together with obvious micro-cracks (Fig. 9c and d) can be found in the matrix. At the same time, macro-twinned martensitic plates become indistinct while some micro-twinned martensite still can be observed (Fig. 9d). However, when more Si is introduced into the rapidly solidified Ti₅₀Ni₅₀ binary alloy, the amount of B2 TiNi austenite appears to be reduced while the amount of TiNi martensite as well as Ti₄Ni₄Si₇ intermetallics becomes larger. The Ti₄Ni₄Si₇ intermetallic compounds precipitate at the grain boundaries while the TiNi dendrites also become finer with increasing Si content. During deformation, a few martensitic plates still can be observed (Fig. 9e) just after the elastic deformation regime and the twinned structures become gradually less prominent with further increasing applied stress (Fig. 9f). Subsequently, some cracks start to appear and link with each other (Fig. 9g and h), resulting in fracture. Hence, as mentioned above, both the yield strength and the fracture strength first decrease and then increase when the Si content increases from 0 to 10 at.%

4. Conclusions

In this work, the microstructure, the martensitic transformation behavior, and the mechanical properties of Ti_{50-x/2}Ni_{50-x/2}Hf_x ($x = 0, 2, 4, 6, 8, 10, \text{ and } 12$ at.%) and Ti_{50-y/2}Ni_{50-y/2}Si_y ($y = 0, 1, 2, 3, 5, 7, \text{ and } 10$ at.%) SMAs prepared by rapid solidification were investigated. The results can be summarized as follows:

1. With increasing Hf content, (Ti,Hf)₂Ni intermetallic compounds gradually precipitate at the interdendritic regions while the dendritic matrix is composed of B2 TiNi and B19' TiNi phases. The amount of B2 and B19' phases gradually decreases when the Hf content increases from 0 to 12 at.%. Minor Si additions stabilize the B2 TiNi phase in the rapidly solidified Ti-Ni-Si alloys, but B2 TiNi crystals gradually transform into B19' TiNi martensites for high Si additions. Besides, some Ti₄Ni₄Si₇ intermetallic compounds and TiNi crystals gradually gather in the interdendritic region as a eutectic structure.
2. A two-stage phase transformation path or/and a one-stage process can be observed in the rapidly solidified Ti-Ni-Hf and Ti-Ni-Si alloys, which can be attributed to variations in the chemical compositions and internal stresses in the TiNi matrix close to and far from Ti₂Ni or Ti₄Ni₄Si₇ precipitates. With increasing number of thermal cycles, the M_s temperature decreases slightly for small amounts of Hf and then rises with further increasing Hf content for the rapidly solidified Ti-Ni-Hf alloys. For the rapidly solidified Ti-Ni-Si alloys, the M_s temperature also de-

creases with increasing number of thermal cycles when the content of Si is below 3 at.%. For more than 3 at.% Si, the M_s temperature remains almost constant. Furthermore, the phase transformation temperature shifts to higher temperatures with decreasing values of e_v/a and c_v when the content of Hf ranges between 0 and 12 at.% or the content of Si is between 0 and 3 at.%. However, when the Si content exceeds 3 at.%, the phase transformation temperature gradually increases with both increasing e_v/a and c_v , which can be correlated with the precipitation of some Ti₄Ni₄Si₇ intermetallics in the Ti-Ni-Si alloys containing more Si.

3. The mechanical properties of the rapidly solidified Ti_{50-x/2}Ni_{50-x/2}Hf_x ($x = 0, 2, 4, 6, 8, 10, \text{ and } 12$ at.%) and Ti_{50-y/2}Ni_{50-y/2}Si_y ($y = 1, 2, 3, 5, 7, \text{ and } 10$ at.%) SMAs were also investigated. The yield strength increases, but the fracture strength and the plasticity decrease with rising Hf or Si content. The details of the deformation behavior strongly depend on the ratio of B2 and B19' TiNi crystals as well as on the precipitation of Ti₂Ni and Ti₄Ni₄Si₇ intermetallic compounds. During deformation, austenites transform into twinned martensites, and the twinned martensites become detwinned with the help of a high density of dislocations while slip bands appear at the interdendritic regions and gradually evolve into micro-cracks. The present results show that when the Si or Hf content is controlled well, good mechanical properties, i.e., relatively high yield strength and large ductility, can be achieved.

Acknowledgments

The authors are grateful to K.L. Wang, J.Mi, Y.Q. Xin, and S.P. Hu for technical assistance and discussions. This work was supported by the National Natural Science Foundation of China (51501103), the German Science Foundation (DFG) under the Leibniz Program (EC 111/26-1), the European Research Council under the ERC Advanced Grant INTELHYB (ERC-2013-ADG-340025), and the Young Scholars Program of Shandong University at Weihai.

References

1. G. Welsch, R. Boyer, and E.W. Collings, Ed., *Materials Properties Handbook: Titanium Alloys*, ASM International, USA, 1994
2. J. Mohd Jani, M. Leary, A. Subic, and M.A. Gibson, A Review of Shape Memory Alloy Research, Applications and Opportunities, *Mater. Des.*, 2014, **56**, p 1078–1113
3. K. Otsuka and X. Ren, Physical Metallurgy of Ti-Ni-Based Shape Memory Alloys, *Prog. Mater. Sci.*, 2005, **50**, p 511–678
4. K. Otsuka and X. Ren, Recent Developments in the Research of Shape Memory Alloys, *Intermetallics*, 1999, **7**, p 511–528
5. Q. Sun, R. Matsui, K. Takeda, and E.A. Pieczyska, Ed., *Advances in Shape Memory Materials*, Springer, Cham, 2017
6. S. Miyazaki and K. Otsuka, Deformation and Transition Behavior Associated with the R-Phase in Ti-Ni Alloys, *Metall. Trans. A*, 1986, **17A**, p 53–63
7. J. Frenzel, J. Pfitzing, K. Neuking, and G. Eggeler, On the Influence of Thermomechanical Treatments on the Microstructure and Phase Transformation Behavior of Ni-Ti-Fe Shape Memory Alloys, *Mater. Sci. Eng. A*, 2008, **481-482**, p 635–638

8. M. Nishida, C.M. Wayman, and T. Honma, Phase Transformations in a $\text{Ti}_{50}\text{Ni}_{47.5}\text{Fe}_{2.5}$ Shape Memory Alloy, *Metallography*, 1986, **19**, p 99–113
9. S.F. Hsieh and S.K. Wu, A Study on a $\text{Ti}_{52}\text{Ni}_{47}\text{Al}_1$ Shape Memory Alloy, *J. Mater. Sci.*, 1999, **34**, p 1659–1665
10. S.F. Hsieh and S.K. Wu, A Study on the Nickel-Rich Ternary Ti-Ni-Al Shape Memory Alloys, *J. Mater. Sci.*, 1997, **32**, p 989–996
11. T.H. Nam, T. Saburi, and Y. Kawamura, Shape Memory Characteristics Associated with the $\text{B2} \rightleftharpoons \text{B19}$ and $\text{B19} \rightleftharpoons \text{B19}'$ Transformations in a Ti-40Ni-10Cu (at.%) Alloy, *Mater. Trans.*, 1990, **31**, p 262–269
12. T.H. Nam, T. Saburi, and K.I. Shimizu, Cu-Content Dependence of Shape Memory Characteristics in Ti-Ni-Cu Alloys, *Mater. Trans.*, 1990, **31**, p 959–967
13. A.S. Paulas, J.P.H.G. Canejo, R.M.S. Martins, and F.M. Braz, Fernandes, Effect of Thermal Cycling on the Transformation Temperatures of Ti-Ni Alloys, *Mater. Sci. Eng. A*, 2004, **378**, p 92–96
14. X.L. Meng, W. Cai, F. Chen, and L.C. Zhao, Effect of Aging on Martensitic Transformation and Microstructure in Ni-Rich TiNiHf Shape Memory Alloy, *Scr. Mater.*, 2006, **54**, p 1599–1604
15. S.F. Hsieh and S.K. Wu, Room-Temperature Phases Observed in $\text{Ti}_{53-x}\text{Ni}_{47}\text{Zr}_x$ High-Temperature Shape Memory Alloys, *J. Alloys Compd.*, 1998, **266**, p 276–282
16. S. Han, W. Zou, S. Jin, Z. Zhang, and D. Yang, The Studies of the Martensite Transformations in a $\text{Ti}_{36.5}\text{Ni}_{48.5}\text{Hf}_{15}$ Alloy, *Scr. Metall. Mater.*, 1995, **32**, p 1441–1446
17. S.F. Hsieh and S.K. Wu, A Study on Ternary Ti-Rich TiNiZr Shape Memory Alloys, *Mater. Charact.*, 1998, **41**, p 151–162
18. S. Sanjabi, Y.Z. Cao, and Z.H. Barber, Multi-Target Sputter Deposition of $\text{Ni}_{50}\text{Ti}_{50-x}\text{Hf}_x$ Shape Memory Thin Films for High Temperature Microactuator Application, *Sens. Actuat. A Phys.*, 2005, **121**, p 543–548
19. Y.X. Tong, P.C. Jiang, F. Chen, B. Tian, L. Li, Y.F. Zheng, D.V. Gunderov, and R.Z. Valiev, Microstructure and Martensitic Transformation of an Ultrafine-Grained TiNiNb Shape Memory Alloy Processed by Equal Channel Angular Pressing, *Intermetallics*, 2014, **49**, p 81–86
20. S.S. Leu, Y.C. Chen, and R.D. Jean, Effect of Rapid Solidification on Mechanical Properties of Cu-Al-Ni Shape Memory Alloys, *J. Mater. Sci.*, 1992, **27**, p 2792–2798
21. G.A. Lara-Rodriguez, G. Gonzalez, H. Flores-Zúñiga, and J. Cortés-Pérez, The Effect of Rapid Solidification and Grain Size on the Transformation Temperatures of Cu-Al-Be Melt Spun Alloys, *Mater. Charact.*, 2006, **57**, p 154–159
22. K.P. Gupta, The Hf-Ni-Ti (Hafnium-Nickel-Titanium) System, *J. Phase Equilib.*, 2001, **22**, p 69–72
23. A. Sibirev, S. Belyaev, and N. Resnina, Unusual Multistage Martensitic Transformation in TiNi Shape Memory Alloy After Thermal Cycling, *Mater. Sci. Forum*, 2013, **738**, p 372–376
24. T.H. Nam, J.H. Kim, M.S. Choi, Y.W. Kim, H.J. Im, J.S. Ahn, and T. Mitani, R Phase Transformation in Equiatomic TiNi Alloy Ribbons Fabricated by Rapid Solidification, *J. Mater. Sci. Lett.*, 2002, **21**, p 685–688
25. Y. Tong, F. Chen, B. Tian, L. Li, and Y. Zheng, Microstructure and Martensitic Transformation of $\text{Ti}_{49}\text{Ni}_{51-x}\text{Hf}_x$ High Temperature Shape Memory Alloys, *Mater. Lett.*, 2009, **63**, p 1869–1871
26. R. Nagarajan and K. Chattopadhyay, Intermetallic $\text{Ti}_2\text{Ni}/\text{TiNi}$ Nanocomposite by Rapid Solidification, *Acta Metall. Mater.*, 1994, **42**, p 947–958
27. W.A. Elliott, F.P. Gagliano, and G. Krauss, Rapid Cooling by Laser Melt Quenching, *Appl. Phys. Lett.*, 1972, **21**, p 23–25
28. J. Khalil-Allafi, G. Eggeler, W.W. Schmahl, and D. Sheptyakov, Quantitative Phase Analysis in Microstructures Which Display Multiple Step Martensitic Transformations in Ni-Rich NiTi Shape Memory Alloys, *Mater. Sci. Eng. A*, 2006, **438**, p 593–596
29. J. Khalil-Allafi, G. Eggeler, A. Dlouhy, W.W. Schmahl, and C. Somsen, On the Influence of Heterogeneous Precipitation on Martensitic Transformations in a Ni-Rich NiTi Shape Memory Alloy, *Mater. Sci. Eng. A*, 2004, **378**, p 148–151
30. K. Otsuka and C.M. Wayman, Ed., *Shape Memory Materials*, Cambridge University Press, Cambridge, 1998
31. S. Miyazaki, Y. Igo, and K. Otsuka, Effect of Thermal Cycling on the Transformation Temperatures of Ti-Ni Alloys, *Acta Metall.*, 1986, **34**, p 2045–2051
32. J. Perkins and W. Muesing, Martensitic Transformation Cycling Effects in Cu-Zn-Al Shape Memory Alloys, *Metall. Mater. Trans. A*, 1983, **14**, p 33–36
33. J.C. Li and G. Ansell, The Effect of Thermal Cycling on the Thermoelastic Martensitic Transformation in a Cu-Zn-Al Alloy, *Metall. Mater. Trans. A*, 1983, **14**, p 1293–1297
34. F. Frank, On Spontaneous Asymmetric Synthesis, *Biochim. Biophys. Acta*, 1953, **11**, p 459–463
35. R.C. Pond, S. Celotto, and J.P. Hirth, A Comparison of the Phenomenological Theory of Martensitic Transformations with a Model Based on Interfacial Defects, *Acta Mater.*, 2003, **51**, p 5385–5398
36. P. McCormick and Y. Liu, Thermodynamic Analysis of the Martensitic Transformation in NiTi-II. Effect of Transformation Cycling, *Acta Metall. Mater.*, 1994, **42**, p 2407–2413
37. J. Olbricht, A. Yawny, A.M. Condó, F.C. Lovey, and G. Eggeler, The Influence of Temperature on the Evolution of Functional Properties During Pseudoelastic Cycling of Ultra Fine Grained NiTi, *Mater. Sci. Eng. A*, 2008, **481**, p 142–145
38. S. Miyazaki, T. Imai, Y. Igo, and K. Otsuka, Effect of Cyclic Deformation on the Pseudoelasticity Characteristics of Ti-Ni Alloys, *Metall. Trans. A*, 1986, **17**, p 115–120
39. P.L. Potapov, A.V. Shelyakov, A.A. Gulyaev, E.L. Svistunova, N.M. Matveeva, and D. Hodgson, Effect of Hf on the Structure of Ni-Ti Martensitic Alloy, *Mater. Lett.*, 1997, **32**, p 247–250
40. V.G. Pushin, N.N. Kuranova, A.V. Pushin, A.N. Uksusnikov, and N.I. Kourov, Structure and Thermoelastic Martensitic Transformations in Ternary Ni-Ti-Hf Alloys with a High-Temperature Shape Memory Effect, *Tech. Phys.*, 2016, **61**, p 1009–1014
41. J.H. Kim, M.S. Choi, and T.H. Nam, Phase Transformation Behavior and Shape Memory Characteristics of Ti-Ni-Si Alloys, *Met. Mater. Int.*, 2001, **7**, p 207–212
42. S.F. Hsieh, S.K. Wu, and H.C. Lin, Transformation Temperatures and Second Phases in Ti-Ni-Si Ternary Shape, *J. Alloys Compd.*, 2002, **339**, p 162–166
43. K.M. Ibrahim, N. Elbagoury, and Y. Fouad, Microstructure and Martensitic Transformation of Cast TiNiSi Shape Memory Alloys, *J. Alloys Compd.*, 2011, **509**, p 3913–3916
44. M. Zarinejad and Y. Liu, Dependence of Transformation Temperatures of NiTi-Based Shape-Memory Alloys on the Number and Concentration of Valence Electrons, *Adv. Funct. Mater.*, 2008, **18**, p 2789–2794
45. G. Jakob, T. Eichhorn, M. Kallmayer, and H.J. Elmers, Correlation of Electronic Structure and Martensitic Transition in Epitaxial Ni_2MnGa Films, *Phys. Rev. B*, 2007, **76**, p 174407
46. J.J. Gilman, R.W. Cumberland, and R.B. Kaner, Design of Hard Crystals, *Int. J. Refract. Met. Hard Mater.*, 2006, **24**, p 1–5
47. J. Gilman, *Electronic Basis of the Strength of Materials*, 1st ed., Cambridge University Press, Cambridge, 2003
48. E.M. Mazzer, P. Gargarella, C.S. Kiminami, C. Bolfarini, R.D. Cava, and M. Galano, On the Valence Electron Theory to Estimate the Transformation Temperatures of Cu-Al-Based Shape Memory Alloys, *J. Mater. Res.*, 2017, **32**, p 1–10
49. T. Fukuda, T. Saburi, K. Doi, and S. Nenno, Nucleation and Self-Accommodation of the R-Phase in Ti-Ni Alloys, *Mater. Trans.*, 1992, **33**, p 271–277